J. Adhesion, 1994, Vol. 45, pp. 105–124
Reprints available directly from the publisher
Photocopying permitted by license only

Printed in the United States of America

The Effects of Interphase Properties on Interfacial Shear Strength in Polymer Matrix Composites*

N. R. SOTTOS** and L. LI

Department of Theoretical and Applied Mechanics, University of Illinois at Urbana-Champaign, Urbana, IL 61801

G. AGRAWAL

Department of Material Science and Engineering, University of Illinois at Urbana-Champaign, Urbana, IL 61801

(Received March 11, 1993; in final form May 6, 1993)

The effects of interphase elastic modulus, glass transition temperature, and thickness on interfacial shear strength were investigated both experimentally and theoretically. Single fiber fragmentation tests were performed over a range of temperatures on samples with tailored interphases. Three different types of interphases were investigated: high modulus/high glass transition temperature, low modulus/low glass transition temperature and uncoated (no tailored interphase). A reduction in interfacial shear strength with temperature was observed for all three types of samples tested. The magnitude of this decrease was found to correlate with the glass transition temperature of the interphase. The low T_g interphase samples showed large reductions in IFSS, while samples with a higher T_g coating showed only a small decrease. A three-phase, axisymmetric elasticity solution was developed to predict the sensitivity of the stress state to the interphase material properties and temperatures used in the experimental studies. Predictions which incorporated the change in modulus of both the matrix and interphase with temperature were in good agreement with the experimental trends. Both the theoretical and experimental results supported the existence of an interphase with reduced glass transition in the uncoated samples.

KEY WORDS fiber/matrix interface; fiber/matrix interphase; effect of glass transition temperature on interfacial shear strength; effect of interphase modulus and thickness on interfacial shear strength; tailored interphases; three-phase axisymmetric elasticity solution.

1. INTRODUCTION

In a composite material, the fiber/matrix interface serves as the critical region where stresses acting on the matrix are transferred to the fibers. For many years, the influence of interfacial bond strength and level of adhesion has been investigated

*Presented at the International Symposium on "The Interphase" at the Sixteenth Annual Meeting of The Adhesion Society, Inc., Williamsburg, Virginia, U.S.A., February 21–26, 1993.

**Corresponding Author.

for graphite/epoxy systems. However, it is widely believed that an interphase region with properties that differ from those of the neat matrix is developed at the fiber/matrix interface.[1] If an interphase exists, the load transfer efficiency will depend not only on the effectiveness of the bond between fiber and matrix but also on: (1) the strength, elastic modulus and coefficient of thermal expansion of the fiber, (2) the elastic modulus and coefficient of thermal expansion of the interphase and (3) the elastic modulus and coefficient of thermal expansion of the matrix. In order to understand the influence of these properties on load transfer, both experimental and theoretical analyses must be performed which systematically vary these parameters.

Several different methods for measuring the stress state and the strength of the bond at the interface have appeared in the literature. One of the most common measurements of adhesion is the single fiber fragmentation test. This method was originally developed by Kelly and Tyson[2] for metals but has since been adopted by Fraser *et al.*,[3] Drzal *et al.*[4] and many others for determining the interfacial shear strength in advanced polymer composites. Many research groups have utilized the single fiber fragmentation test to investigate the influence of different matrices, fibers, and various fiber surface treatments on adhesion in carbon/epoxy systems. Others, most notably Drzal,[5,6,7] have performed extensive experimental investigations to understand the effects of adhesion (measured by single fiber fragmentation) on the mechanical behavior of carbon/epoxy composites. However, little is understood about how the thermo-mechanical properties of a distinct interphase region influence the adhesion measured by single fiber fragmentation tests.

Temperature has also been shown to have a significant effect on the interfacial shear strength predicted by the single fiber fragmentation test.[8–15] In each of these investigations, an increase in critical length was observed with increasing temperature. References[8,10,15] noted that the resulting decrease in interfacial shear strength occurred at temperatures lower than the glass transition temperature of the matrix, indicating the presence of an interphase layer with different properties. The thermal stresses caused by changes in temperature also have a significant influence on the interfacial shear strength.

Numerous analytical models have been developed to understand the stress transfer in fiber fragmentation tests. Early models by Cox,[16] Dow[17] and Rosen[18] utilized an elastic shear lag analysis to predict the shear stress along the length of an embedded filament. Kelly and Tyson[19] developed an elastic-plastic analysis which assumed a constant interfacial shear stress. While References 16–19 assumed perfect bonding, others explored shear lag models which assumed partial debonding or total debonding.[20,21,22] Others have utilized a stress function approach to predict more accurately the axisymmetric stress distribution around an isolated fiber fragment.[23,24,25] More recently, Nairn[26] developed a three-dimensional axisymmetric solution for the stresses around breaks in an embedded fiber using variational mechanics. This work provides an excellent comparison of the more advanced solution with shear lag analysis. Several finite element analyses of the stress state around embedded fiber fragments have also been carried out.[27,28] While these models have aided in interpreting the results of embedded single fiber tests, none considered the influence of a distinct interphase region.

Several other works have applied shear lag analysis to a three-phase (fiber, matrix and interphase) system.[29,30,31] The extension of shear lag analysis to include an interphase region, however, requires major assumptions about the behavior or properties of the interphase region. For example, Lhotellier and Brinson[29] assume that the interphase carries a fraction of the tensile load and a fraction of the matrix shear stress, while Theocaris[14] assumes the interphase carries only shear stresses. The need exists for a more exact elasticity solution to understand effectively the role of the interphase in determining interfacial shear strength.

In the current work, the influence of interphase elastic modulus, glass transition temperature, and thickness on interfacial shear strength were investigated both experimentally and theoretically. Single fiber critical length tests were performed on carbon/epoxy samples with tailored interphases over a range of temperatures. A three-phase, axisymmetric elasticity solution was developed to predict the sensitivity of the stress state to the interphase material properties and temperatures used in the experimental studies. A comparison of theoretical and experimental results was utilized to assess the role of interphase properties on load transfer.

2. EXPERIMENTAL OBSERVATIONS

Single fiber critical length tests were performed over a range of temperatures on samples with tailored interphases to assess the influence of interphase modulus and glass transition temperature on the interfacial shear strength. Three different types of interphases were investigated: low modulus/low glass transition temperature, higher modulus/higher glass transition temperature, and uncoated.

2.1 Sample Preparation and Procedure

Single fiber critical length specimens consisted of a Hercules AS4 carbon fiber embedded in an epoxy matrix. Shell EPON 828® (diglycidyl ether of bisphenol A) resin cured with AMICURE PACM® [bis(p-amino cyclohexyl) methane] was chosen for the matrix material. Samples with three different interphases were prepared. In the first type of sample (type I), the AS4 fibers were left uncoated. For the second type of sample (type II), AS4 fibers were coated with an approximately 1 micron thick layer of EPON 871® resin to reduce the glass transition and modulus of the interphase. EPON 871 (aliphatic polyepoxide) is an amber, low viscosity liquid which imparts increased flexibility to EPON 828 compositions. The fibers were coated by gently pulling single filaments through a bath of the resin. For the third type of sample (type III), fibers were coated with an approximately one micron thick layer of a stoichiometric mix of EPON Resin DPS-164® (epoxy cresol novolac) and PACM to obtain an interphase of higher glass transition temperature and modulus. The solid DPS 164 was first dissolved in acetone, then mixed with PACM. After evaporating the acetone, the coating was cured on the fibers.

The Young's modulus measured by room temperature tensile tests and glass transition temperature measured by DSC (Differential Scanning Calorimetry) for the matrix and coatings are listed in Table I. All fibers were washed in isopropyl alcohol

TABLE I
Properties of matrix and coatings

Resin	E (GPa)	T_g (°C)
Neat Matrix—(EPON 828+PACM)	2.5	160
Coating II—(EPON 871+828+PACM)	2.1	80
Coating III—(EPON DPS-164+PACM)	3.5	150

to remove any surface lubricants or contaminants and allowed to dry. Coated or uncoated single fibers were then embedded in dog bone coupons of the stoichiometric mix of the matrix (28 parts PACM to 100 parts EPON 828) as described by Drzal *et al.*[4] The single fiber dog bone specimens were cured for 1 hour at 80°C and 1 hour at 150°C and then allowed to cool to room temperature slowly to minimize residual stresses.

Once fabricated, the samples were loaded in tension using a small hand-operated tensile apparatus so that the fiber fractured into small pieces within the matrix. The fracture process continued until the fiber pieces reached a minimum critical length. The fiber lengths as well as the fiber diameter were then carefully measured under the microscope. Samples were tested at room temperature, 60°C, 80°C, and 100°C. Temperatures above 100°C were not considered. Elevated temperatures tests were performed in a temperature-controlled oven normally used for full scale mechanical testing and the specimens were then examined under the microscope. Fifteen samples were tested at each temperature.

According to the elastic-plastic shear lag analysis of Kelly,[2] the interfacial shear strength, τ, is inversely proportional to the critical length and is expressed as

$$\tau = \frac{\sigma_f d}{2 l_c} \tag{1}$$

where l_c is the critical length, d is the fiber diameter, and σ_f is the fiber strength. However, if many samples are tested the data can be fitted to a two-parameter Weibull distribution. The mean interfacial shear strength is calculated by the relation[4]

$$\tau = \frac{\sigma_f}{2\beta}\Gamma\left(1 - \frac{1}{\alpha}\right) \tag{2}$$

The parameters α and β are solutions to

$$\beta = \left(\frac{1}{n}\sum X_i\right)^{\frac{1}{\alpha}} \tag{3}$$

$$\frac{\sum X_i^\alpha}{\ln(\sum X_i)} \sum X_i^\alpha - \frac{1}{\alpha} - \frac{\ln(\sum X_i)}{n} = 0 \tag{4}$$

where $X_i = \frac{l_c}{d}$, n is the number of measurements, and Γ is the gamma function.

2.2 Test Results and Discussion

The interfacial shear strengths (IFSS) measured at room temperature for the three different types of samples are listed in Table II. The interfacial shear strengths were calculated using Eq.(2) and a fiber strength of $\sigma_f = 4.7$ GPa. Type II (low T_g) had a slightly higher IFSS than the value measured for type I samples (no coating), while the type III (higher T_g) samples had a lower IFSS. Overall, the addition of the coatings had only a small effect on IFSS at room temperature.

The influence of temperature on the fragmentation test results is summarized in Figure 1. IFSS is plotted as a function of temperature for all three types of samples. All values of IFSS have been normalized by the value at room temperature for each particular type of sample (τ_o). A decrease in IFSS with temperature is observed for all three samples. Heating to a moderate temperature of 60°C caused a 15% reduction in IFSS for type II (lower T_g coating) samples, a 10% reduction for type I (no

TABLE II
Room temperature IFSS

Sample type	τ_o (MPa)
I	44.2
II	45.2
III	40.0

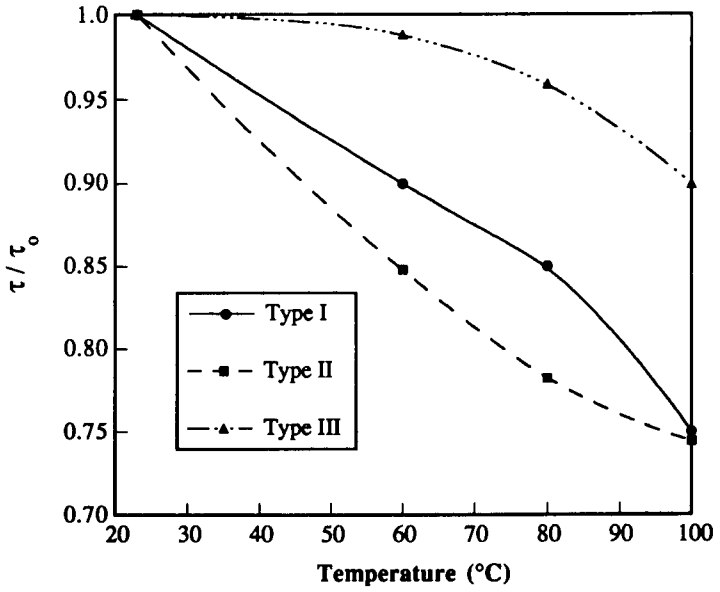

FIGURE 1 Variation of normalized interfacial shear strength (τ/τ_o) with temperature for the three types of samples.

coating) and no reduction in IFSS for type III (higher T_g coating) samples. At intermediate temperatures (80–85°C), the value of IFSS decreased by 22% for type II samples and 15% for type I, while the value for type III samples only decreased about 4%. Heating to 100°C caused nearly a 26% reduction in IFSS for both type I and type II samples. Only a 10% decrease in IFSS was recorded for type III samples. The reversal in curvature observed for type II (low T_g coating) samples is consistent with the results of Wimolkiatisak and Bell[10] suggesting that the failure in these samples is more interphase/matrix dominated than interface dominated.

The observed decrease in IFSS with increasing temperature for type I and II samples is consistent with the results of previous studies.[8–15] Ohsawa *et al.*[11] found the critical length of a glass fiber in epoxy resin significantly increased with temperature, causing a corresponding decrease in IFSS. The authors concluded that the decreasing values could not be explained solely by thermal stresses between the fiber and matrix and suggested that this phenomenon was brought about by a decrease in the shear strength of the matrix. The Ohsawa tests were performed in a range from 40°C–100°C, while the glass transition temperature of the epoxy matrix was 60°C. In other investigations,[8,9,15] the single fiber fragmentation tests were performed at temperatures below the T_g of the neat matrix. Reductions in IFSS were observed at temperatures far below the T_g of the neat resin where no appreciable softening of the resin should have occurred.

In the current work, a comparison of the T_g measured for the coatings and resin listed in Table I with the reductions in IFSS observed in Figure 1, provides considerable insight into the nature of interphase glass transition. As the interphase passes through its glass transition, there is an order of magnitude drop in elastic modulus and a sudden drop in the ability to transfer load. Also, a large decrease in the radial, compressive residual stresses around the fiber occurs due to the very low interphase modulus. Both of these factors are reflected by an increase in critical length and an associated drop in IFSS at temperatures near the interphase T_g.

Only small reductions in IFSS were measured for type III samples which had a tailored interphase with a T_g of 150°C. Large reductions in IFSS (15%) were recorded at 60°C for type II samples which had a tailored interphase with a T_g of approximately 80°C. The behavior of these two sample types is somewhat intuitive given the relationship of their known interphase T_g in relation to the test temperature. The behavior of the uncoated type I samples is less intuitive and has interesting implications. Significant reductions in IFSS were observed around 80°C, far from the glass transition temperature of the neat resin (160°C). These results tend to support the existence of an interphase in the untreated sample, which has a reduced glass transition temperature. Previous interferometric studies by Sottos[15,32] also support this conclusion. The existence of a lower T_g region near the fiber surface could have a significant effect on the thermal stability and toughness of the overall composite.

3. THEORETICAL PREDICTIONS

The single fiber critical length test results demonstrated that the properties of the interphase, in particular T_g, have a significant effect on IFSS. In order to interpret

these results and to understand better the influence of the interphase, a three-phase composite cylinder elasticity solution was developed to predict the stress transfer for a single fiber embedded in a polymer matrix under thermo-mechanical loading.

3.1 Problem Formulation

A schematic of the three-phase composite cylinder used for the analysis is shown in Figure 2. This axially-symmetric, thermoelastic problem is analyzed by using linear thermoelasticity theory. The interphase is treated as a region with uniform material properties, different from those of the matrix or the fiber.

In cylindrical coordinates, the axially-symmetric state of stress is characterized by the conditions $\sigma_{r\theta}=\sigma_{z\theta}=0, \frac{\partial}{\partial\theta}=0$. The general equations of equilibrium, in the absence of body force, reduce to the form

$$\left.\begin{aligned} &\frac{\partial\sigma_{rr}^{(i)}}{\partial r}+\frac{\partial\sigma_{rz}^{(i)}}{\partial z}+\frac{\sigma_{rr}^{(i)}-\sigma_{\theta\theta}^{(i)}}{r}=0 \\ &\frac{\partial\sigma_{rz}^{(i)}}{\partial r}+\frac{\partial\sigma_{zz}^{(i)}}{\partial z}+\frac{\sigma_{rz}^{(i)}}{r}=0 \end{aligned}\right\} \quad (i=1,2,3) \tag{5}$$

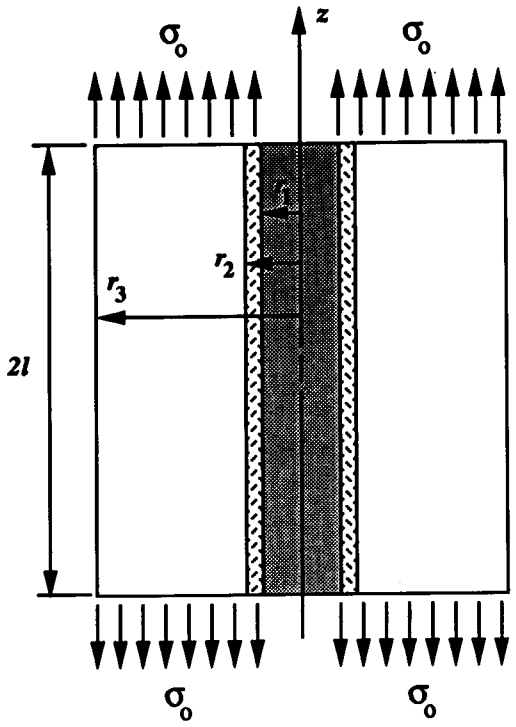

FIGURE 2 Schematic of the three-phase composite cylinder model.

The strain-displacement relations in cylindrical coordinates are

$$\epsilon_{rr}^{(i)} = \frac{\partial u^{(i)}}{\partial r}, \quad \epsilon_{\theta\theta}^{(i)} = \frac{u^{(i)}}{r}, \quad \epsilon_{zz}^{(i)} = \frac{\partial w^{(i)}}{\partial z}$$
$$\epsilon_{rz}^{(i)} = \frac{\partial u^{(i)}}{\partial z} + \frac{\partial w^{(i)}}{\partial r} \tag{6}$$

and the stress-strain-temperature relations are given by

$$\begin{cases} \sigma_{rr}^{(i)} = \lambda^{(i)} e^{(i)} + 2G^{(i)} \epsilon_{rr}^{(i)} - \dfrac{E^{(i)} \alpha^{(i)} T}{1 - 2\nu^{(i)}} \\ \sigma_{\theta\theta}^{(i)} = \lambda^{(i)} e^{(i)} + 2G^{(i)} \epsilon_{\theta\theta}^{(i)} - \dfrac{E^{(i)} \alpha^{(i)} T}{1 - 2\nu^{(i)}} \\ \sigma_{zz}^{(i)} = \lambda^{(i)} e^{(i)} + 2G^{(i)} \epsilon_{zz}^{(i)} - \dfrac{E^{(i)} \alpha^{(i)} T}{1 - 2\nu^{(i)}} \\ \sigma_{rz}^{(i)} = G^{(i)} \epsilon_{rz}^{(i)} \end{cases} \tag{7}$$

where $\alpha^{(i)}$ is the coefficient of thermal expansion, T(r,z) is the temperature, $\lambda^{(i)} = \dfrac{\nu^{(i)} E^{(i)}}{(1+\nu^{(i)})(1-2\nu^{(i)})}$ and $G^{(i)} = \dfrac{E^{(i)}}{2(1+\nu^{(i)})}$.

Substitution of the stress-strain-temperature relations and the strain-displacement relations into the equilibrium gives the governing equations in terms of displacements

$$\left.\begin{aligned} &\nabla^2 u^{(i)} - \frac{u^{(i)}}{r^2} + \frac{1}{1-2\nu^{(i)}} \frac{\partial e^{(i)}}{\partial r} - \frac{2(1+\nu^{(i)})}{1-2\nu^{(i)}} \frac{\partial (\alpha^{(i)} T)}{\partial r} = 0 \\ &\nabla^2 w^{(i)} + \frac{1}{1-2\nu^{(i)}} \frac{\partial e^{(i)}}{\partial z} - \frac{2(1+\nu^{(i)})}{1-2\nu^{(i)}} \frac{\partial (\alpha^{(i)} T)}{\partial z} = 0 \end{aligned}\right\} \quad (i = 1,2,3) \tag{8}$$

where

$$\nabla^2 = \frac{\partial^2}{\partial r^2} + \frac{1}{r}\frac{\partial}{\partial r} + \frac{\partial^2}{\partial z^2}$$
$$e^{(i)} = \frac{\partial u^{(i)}}{\partial r} + \frac{u^{(i)}}{r} + \frac{\partial w^{(i)}}{\partial z} \tag{9}$$

3.2 Method of Solution

The solution of the governing equations, Eq. (8), for displacements consists of two parts such that $\underline{u} = \underline{u}_p + \underline{u}_c$ where $\underline{u}_p$ is the particular solution and $\underline{u}_c$ is the complementary solution. The particular solution of the governing equations is obtained through the use of the displacement potential. The complementary solution is achieved by using the Love's stress function. The final solution, the sum of the complementary and particular solutions, must satisfy all the necessary boundary conditions.

3.2.1 Particular Solution The particular solution is obtained by introducing a displacement potential function of the form $\psi^{(i)}(r,z)$ which satisfies the governing equation:

$$\nabla^2\psi^{(i)} = \frac{(1+\nu^{(i)})}{(1-\nu^{(i)})}\alpha^{(i)}T \tag{10}$$

For uniform temperature distribution, T, $\psi^{(i)}(r,z)$ is given by

$$\psi^{(i)}(r,z) = \frac{1}{4}m^{(i)}T\left[\frac{r^2}{2}+z^2\right] \tag{11}$$

where $m^{(i)} = \frac{(1+\nu^{(i)})}{(1-\nu^{(i)})}\alpha^{(i)}$.

The equations relating $\psi^{(i)}(r,z)$ to the particular components of the displacement are well known and given in the Appendix. Substitution of Eq. (11) into Eqs. (A1) in the Appendix yields the following form of the particular displacements and stresses,

$$\begin{cases} u_p^{(i)} = \frac{1}{4}m^{(i)}Tr \\ w_p^{(i)} = \frac{1}{2}m^{(i)}Tz \\ \sigma_{rr\,p}^{(i)} = -\frac{3}{2}G^{(i)}m^{(i)}T \\ \sigma_{\theta\theta p}^{(i)} = -\frac{3}{2}G^{(i)}m^{(i)}T \\ \sigma_{zz\,p}^{(i)} = -G^{(i)}m^{(i)}T \\ \sigma_{rz\,p}^{(i)} = 0 \end{cases} \tag{12}$$

3.2.2 Complementary Solution The complementary solution to Eq. (8) is obtained by using the Love's stress function, provided the stress function $F^{(i)}(r,z)$ satisfies the relation

$$\nabla^2\nabla^2F^{(i)} = 0 \tag{13}$$

It can be shown that the following functions satisfy Eq. (13)

$$\begin{aligned} F_1^{(i)} &= (A^{(i)}r^2 + C^{(i)}\log r)z + B^{(i)}z^3 \\ F_2^{(i)} &= \sum_{n=1}^{\infty} \sin(\mu_n z)[D_{1n}^{(i)}I_o(\mu_n r) + D_{3n}^{(i)}\mu_n r I_1(\mu_n r) + D_{2n}^{(i)}K_o(\mu_n r) + D_{4n}^{(i)}\mu_n r K_1(\mu_n r)] \end{aligned} \tag{14}$$

where I_o, I_1 and K_o, K_1 are the modified Bessel functions of the first and second kind, respectively, while $A^{(i)}$, $B^{(i)}$, $C^{(i)}$, $D_{1n}^{(i)}$, $D_{2n}^{(i)}$, $D_{3n}^{(i)}$ and $D_{4n}^{(i)}$ are constants to be determined by application of the boundary conditions. The μ_n's are the eigenvalues and determined by

$$\mu_n = \frac{n\pi}{2l} \quad (n = 1,3,5,\ldots) \tag{15}$$

The Love's stress function $F^{(i)}(r,z)$ is then made up of $F^{(i)} = F_1^{(i)} + F_2^{(i)}$ which gives the complementary displacements and stresses

$$\begin{cases} u_c^{(i)} = u_{c1}^{(i)} + u_{c2}^{(i)} \\ w_c^{(i)} = w_{c1}^{(i)} + w_{c2}^{(i)} \\ \sigma_{rr\,c}^{(i)} = \sigma_{rr\,c1}^{(i)} + \sigma_{rr\,c2}^{(i)} \\ \sigma_{\theta\theta\,c}^{(i)} = \sigma_{\theta\theta\,c1}^{(i)} + \sigma_{\theta\theta\,c2}^{(i)} \\ \sigma_{zz\,c}^{(i)} = \sigma_{zz\,c1}^{(i)} + \sigma_{zz\,c2}^{(i)} \\ \sigma_{rz\,c}^{(i)} = \sigma_{rz\,c1}^{(i)} + \sigma_{rz\,c2}^{(i)} \end{cases} \tag{16}$$

The expressions relating Love's function to the complementary displacements and stresses are given in the Appendix. Substitution of $F_1^{(i)}$ into Eqs. (A2) in the Appendix yields the first part of the complementary solution

$$\begin{cases} u_{c1}^{(i)} = -\dfrac{1+\nu^{(i)}}{E^{(i)}}\left[2A^{(i)}r + \dfrac{C^{(i)}}{r}\right] \\ w_{c1}^{(i)} = \dfrac{1+\nu^{(i)}}{E^{(i)}}[2(1-\nu^{(i)})(4A^{(i)} + 6B^{(i)}) - 6B^{(i)}]z \\ \sigma_{rr\,c1}^{(i)} = \nu^{(i)}(4A^{(i)} + 6B^{(i)}) + \dfrac{C^{(i)}}{r^2} - 2A^{(i)} \\ \sigma_{\theta\theta\,c1}^{(i)} = \nu^{(i)}(4A^{(i)} + 6B^{(i)}) - \dfrac{C^{(i)}}{r^2} - 2A^{(i)} \\ \sigma_{zz\,c1}^{(i)} = (2-\nu^{(i)})(4A^{(i)} + 6B^{(i)}) - 6B^{(i)} \\ \sigma_{rz\,c1}^{(i)} = 0 \end{cases} \tag{17}$$

The second part of the complementary solution is determined using $F_2^{(i)}$ in a similar fashion

$$\begin{cases} u_{c2}^{(i)} = \displaystyle\sum_{n=1}^{\infty} \cos(\mu_n z)[D_{1n}^{(i)}h_{1n}^{(i)}(r) + D_{3n}^{(i)}h_{2n}^{(i)}(r) + D_{2n}^{(i)}g_{1n}^{(i)}(r) + D_{4n}^{(i)}g_{2n}^{(i)}(r)] \\ w_{c2}^{(i)} = \displaystyle\sum_{n=1}^{\infty} \sin(\mu_n z)[D_{1n}^{(i)}h_{3n}^{(i)}(r) + D_{3n}^{(i)}h_{4n}^{(i)}(r) + D_{2n}^{(i)}g_{3n}^{(i)}(r) + D_{4n}^{(i)}g_{4n}^{(i)}(r)] \\ \sigma_{rr\,c2}^{(i)} = \displaystyle\sum_{n=1}^{\infty} \cos(\mu_n z)[D_{1n}^{(i)}h_{5n}^{(i)}(r) + D_{3n}^{(i)}h_{6n}^{(i)}(r) + D_{2n}^{(i)}g_{5n}^{(i)}(r) + D_{4n}^{(i)}g_{6n}^{(i)}(r)] \\ \sigma_{\theta\theta\,c2}^{(i)} = \displaystyle\sum_{n=1}^{\infty} \cos(\mu_n z)[D_{1n}^{(i)}h_{7n}^{(i)}(r) + D_{3n}^{(i)}h_{8n}^{(i)}(r) + D_{2n}^{(i)}g_{7n}^{(i)}(r) + D_{4n}^{(i)}g_{8n}^{(i)}(r)] \\ \sigma_{zz\,c2}^{(i)} = \displaystyle\sum_{n=1}^{\infty} \cos(\mu_n z)[D_{1n}^{(i)}h_{9n}^{(i)}(r) + D_{3n}^{(i)}h_{10n}^{(i)}(r) + D_{2n}^{(i)}g_{9n}^{(i)}(r) + D_{4n}^{(i)}g_{10n}^{(i)}(r)] \end{cases} \tag{18}$$

$$\sigma_{rz\,c2}^{(i)} = \sum_{n=1}^{\infty} \sin(\mu_n z)[D_{1n}^{(i)} h_{11n}^{(i)}(r) + D_{3n}^{(i)} h_{12n}^{(i)}(r) + D_{2n}^{(i)} g_{11n}^{(i)}(r) + D_{4n}^{(i)} g_{12n}^{(i)}(r)]$$

where $h_{1n}^{(i)}(r) \sim h_{12n}^{(i)}(r)$ are expressions containing r, $I_o(\mu_n r)$ and $I_1(\mu_n r)$, $g_{1n}^{(i)}(r) \sim g_{12n}^{(i)}(r)$ are expressions containing r, $K_o(\mu_n r)$ and $K_1(\mu_n r)$. The functions $h_{1n}^{(i)}(r) \sim h_{12n}^{(i)}(r)$ and $g_{1n}^{(i)}(r) \sim g_{12n}^{(i)}(r)$ are given in the Appendix.

3.2.3 Boundary Conditions Finally, the total stress $\underline{\underline{\sigma}} = \underline{\underline{\sigma}}_p + \underline{\underline{\sigma}}_c$ and total displacements $\underline{u} = \underline{u}_p + \underline{u}_c$ are required to satisfy the boundary conditions. The boundary conditions for the single embedded fiber with interphase shown in Figure 2 are as follows:

(1) At $r = 0$ the solution is bounded.

(2) At $z = \pm 1$ a uniform longitudinal load, σ_o, is applied to the matrix domain and the shear stresses constitute a system in equilibrium.

$$\begin{aligned} \sigma_{zz}^{(1)} &= 0 \\ \sigma_{zz}^{(2)} &= 0 \\ \sigma_{zz}^{(3)} &= \sigma_o \\ \int \sigma_{rz}^{(i)} dr &= 0 \end{aligned} \tag{19}$$

(3) At $r = r_3$ the surface is traction free, *i.e.*

$$\begin{aligned} \sigma_{rr}^{(3)} &= 0 \\ \sigma_{rz}^{(3)} &= 0 \end{aligned} \tag{20}$$

For both the fiber/interphase boundary and the interphase/matrix boundary, continuity of displacements and traction (perfect adhesion) is assumed. Thus the interface boundary conditions are expressed as

(4) At $r = r_1$

$$\begin{aligned} u^{(1)} &= u^{(2)} \\ w^{(1)} &= w^{(2)} \\ \sigma_{rr}^{(1)} &= \sigma_{rr}^{(2)} \\ \sigma_{rz}^{(1)} &= \sigma_{rz}^{(2)} \end{aligned} \tag{21}$$

(5) At $r = r_2$

$$\begin{aligned} u^{(3)} &= u^{(2)} \\ w^{(3)} &= w^{(2)} \\ \sigma_{rr}^{(3)} &= \sigma_{rr}^{(2)} \\ \sigma_{rz}^{(3)} &= \sigma_{rz}^{(2)} \end{aligned} \tag{22}$$

Application of the boundary conditions at $r=0$ yields

$$C^{(1)} = D_{2n}^{(1)} = D_{4n}^{(1)} = 0 \tag{23}$$

The remaining boundary conditions generate two sytems of linear equations which determine the unknown constants $A^{(1)}$, $A^{(2)}$, $A^{(3)}$, $B^{(1)}$, $B^{(2)}$, $B^{(3)}$, $C^{(2)}$, $C^{(3)}$ and $D_{1n}^{(i)}$, $D_{2n}^{(i)}$, $D_{3n}^{(i)}$, $D_{4n}^{(i)}$, respectively.

3.3 Numerical Results

Using the solution method outlined above, predictions are made of the stress state surrounding a single embedded fiber fragment under mechanical loading. Calculations are made assuming the fiber and matrix properties listed in Table III and the following geometrical properties: $r_1 = 4.0\ \mu m$, $r_3 = 10r_1$, $l/r_1 = 50$. Predictions of interfacial shear stress and fiber axial stress for the case of no tailored interphase region and $\Delta T = 0$ are plotted in Figure 3 as a function of distance along the embedded fiber length. The stress values predicted by the current theory are compared with those calculated using shear lag analysis.[16] The current theory predicts a slightly larger value of interfacial shear stress at the fiber end and a lower, constant value of fiber stress in the center of the fiber.

Direct prediction of IFSS from the current theory is not feasible; however, trends in the variation of IFSS due to changes in interphase properties can be assessed. The critical length measured experimentally in a single fiber fragmentation is inversely proportional to the interfacial shear strength and is expressed by rearranging Eq. (1) as follows

$$\frac{1}{l_c} = \frac{2\tau}{d\sigma_f} \tag{24}$$

Although the theoretical analysis predicts only elastic stresses, the ratio of the maximum interfacial shear stress to the maximum fiber axial stress, $\frac{\sigma_{rz\,(max)}}{\sigma_{zz\,(max)}}$, is indicative of the load transfer efficiency from fiber to matrix. Using classical shear lag analysis it is easy to show that this ratio of the maximum elastic stresses is inversely proportional to the critical length.[16,33] Predictions of trends in IFSS are thus made by using the current theory to calculate the ratio, $\frac{\sigma_{rz\,(max)}}{\sigma_{zz\,(max)}}$, for the different interphase properties being investigated. The maximum shear stress always occurs at the fiber ends, $z/l = 1.0$, while the maximum axial stress occurs at the fiber center, $z/l = 0.0$.

TABLE III
Material properties for theoretical predictions

Property	Fiber	Matrix	Interphase
E (GPa)	221	2.5	varied
α ($\times 10^{-6}$/°C)	−0.5	68	68
ν	.25	.33	.33

a)

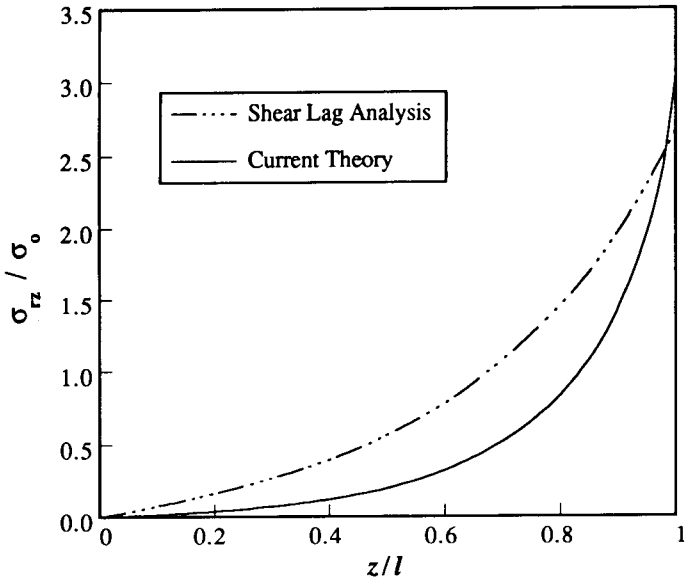

b)

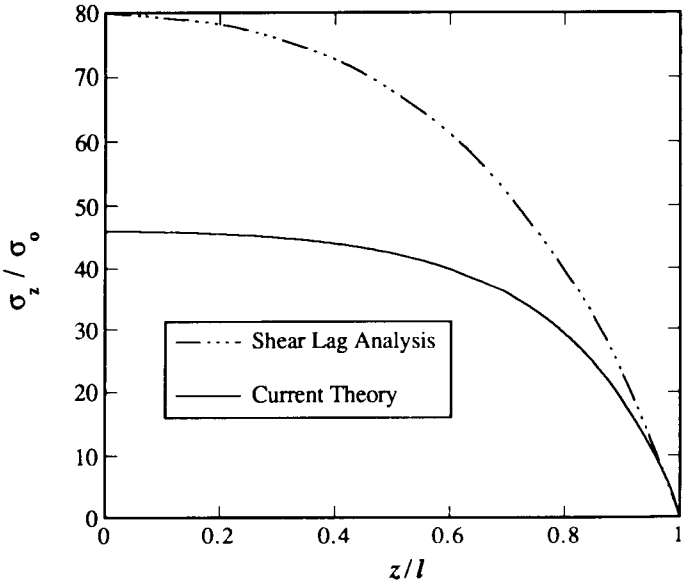

FIGURE 3 Predictions using the current theory and shear lag analysis of a) interfacial shear stress (σ_{rz}/σ_o) b) interfacial fiber axial stress (σ_{zz}/σ_o) as a function of distance along the fiber for no interphase and $\Delta T = 0$.

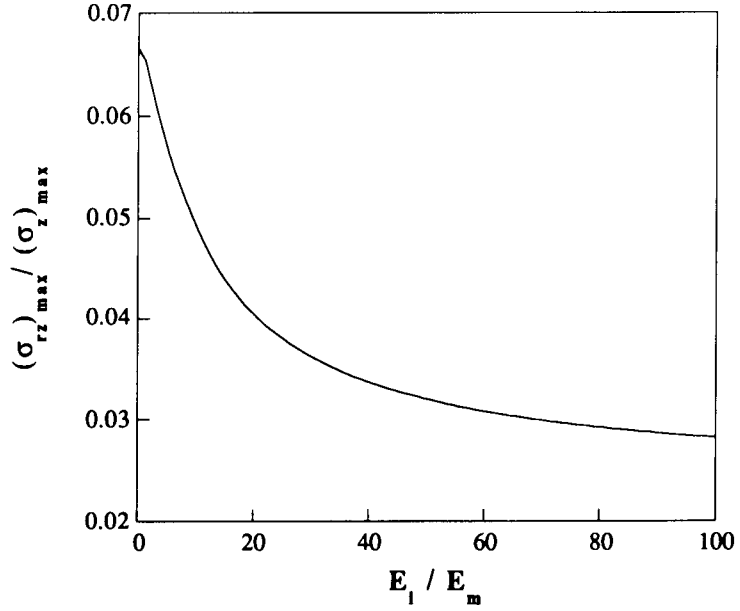

FIGURE 4 Variation of $\frac{\sigma_{rz(max)}}{\sigma_{zz(max)}}$ with interphase modulus for interphase width, $\lambda = 0.2$ microns, an applied load $\sigma_o = 50$ MPa and $\Delta T = 0$.

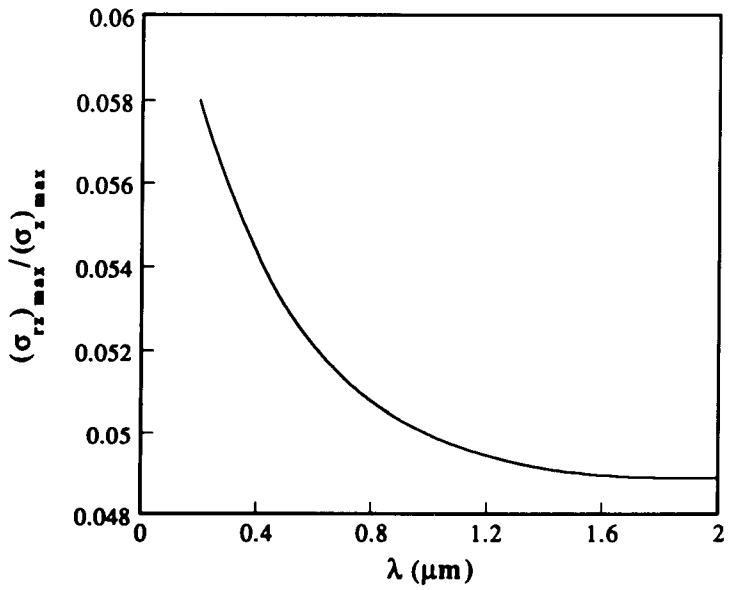

FIGURE 5 Variation of $\frac{\sigma_{rz(max)}}{\sigma_{zz(max)}}$ with interphase width, λ, for a set interphase modulus $E_i = E_m/5$, applied load $\sigma_o = 50$ MPa and $\Delta T = 0$.

A parametric study was carried out to assess systematically the influence of interphase modulus and thickness on the stress state of an embedded fiber fragment. The variation of $\frac{\sigma_{rz\,(max)}}{\sigma_{zz\,(max)}}$ with changing interphase modulus is shown in Figure 4 for an applied load, $\sigma_o = 50$ MPa, and a fixed interphase width, $\lambda = r_2 - r_1 = 0.2$ microns. No thermal loads are considered in these calculations ($\Delta T = 0$), as the effects of temperature are discussed in the following section. The ratio of $\frac{\sigma_{rz(max)}}{\sigma_{zz\,(max)}}$ decreases rapidly with decreasing interphase modulus. Thus, a decrease in IFSS is expected in the presence of a more compliant interphase. The influence of interphase width is shown in Figure 5 for a fixed interphase modulus of $E_i = E_m/5$, where E_i is the interphase modulus and E_m is the modulus of the matrix. As the compliant interphase becomes larger, its effect becomes more pronounced, causing further reductions in IFSS. At large enough widths, the interphase behaves as a single matrix phase.

4. COMPARISON OF THEORY AND EXPERIMENT

A one-to-one comparison of theory and experiment is difficult. As discussed in the previous section, theoretical comparison can be made with the experimental observations of IFSS by calculating the $\frac{\sigma_{rz(max)}}{\sigma_{zz(max)}}$ for the appropriate interphase properties and temperature ranges used in the experiments. The properties of the different interphase coatings as well as the neat matrix were carefully measured over the necessary range of temperatures using fixed frequency Dynamic Mechanical Analysis (DMA). The values of storage modulus for the matrix and the coatings are plotted as a function of temperature in Figure 6. For the stress calculations at a particular temperature, the properties measured at that temperature for both the matrix and the interphase were utilized. Also, a coating thickness (interphase width) of one micron was used for the calculations in the type II and III samples.

Theoretical predictions of $\frac{\sigma_{rz(max)}}{\sigma_{zz(max)}}$ for the three different interphase conditions are shown in Figure 7. The 10% reduction in stress transfer predicted by the theoretical analysis for the type III (higher T_g) samples is in excellent agreement with the experimental trends in Figure 1. The theoretical predictions indicate a 45% decrease in IFSS for type II samples which is in good qualitative agreement with the experimental results although the value of percent reduction is over predicted. The predictions for type I samples using the modulus data for the neat resin in Figure 6 do not show any significant decrease in $\frac{\sigma_{rz(max)}}{\sigma_{zz(max)}}$ as observed experimentally. Due to the high T_g of the neat EPON 828/PACM resin, the measured elastic modulus decreased only slightly at the experimental temperatures leading to only a slight reduction of the ratio in Figure 7. Consequently, the theoretical predictions in Figure 7 also support the existence of an interphase with a reduced glass transition in the uncoated

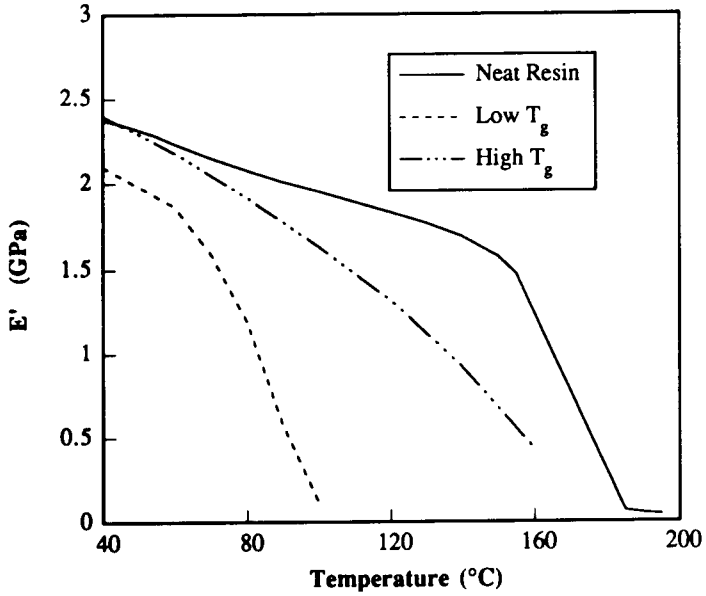

FIGURE 6 Storage modulus as determined by fixed frequency DMA for the matrix and coatings used in the experimental study.

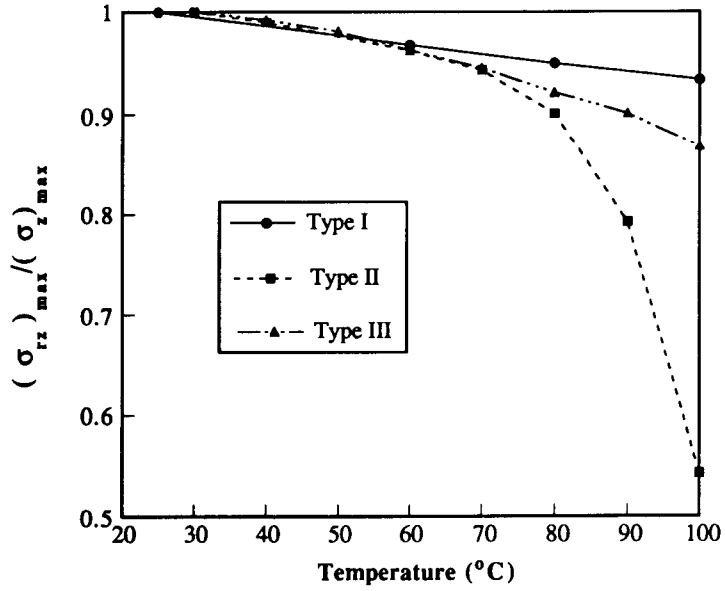

FIGURE 7 Theoretical predictions of $\frac{\sigma_{rz(max)}}{\sigma_{zz(max)}}$ for the three types of samples considered in the experimental study.

fibers. If the predictions for the type I samples are modified to include such an interphase, a decrease in $\frac{\sigma_{rz(max)}}{\sigma_{zz(max)}}$ at moderate temperature is calculated.

Recently, Palmese[34] has measured changes in glass transition temperature as a function of amine concentration for the neat EPON 828/PACM system using both dynamic and thermal mechanical analysis (DMA and TMA). For amine concentrations both above and below the stoichiometric point, the value of T_g was significantly reduced. If the fiber surface were to alter the cure chemistry such that a non-stoichiometric mixture of amine and epoxy occurred, the material in this region would, in theory, have a lower glass transition temperature than the neat resin. The results obtained in the current study tend to support the existence of such an altered interphase region.

5. CONCLUSIONS

The influence of interphase elastic modulus, glass transition temperature, and thickness on interfacial shear strength of single fiber critical length specimens were investigated both experimentally and theoretically. A decrease in IFSS with temperature was observed for all three types of samples tested. For the samples with tailored interphases, the magnitude of this decrease was found to correlate with the glass transition temperature of the coating. Samples with a higher T_g fiber coating showed only a 10% reduction in IFSS at 100°C, while samples with a low T_g coating had a 26% reduction in IFSS. Uncoated samples (no tailored interphase) showed nearly the same reduction in IFSS as the low T_g coated samples at 100°C. These results implied the formation of an interphase with a reduced glass transition temperature in uncoated carbon/epoxy systems.

A three-phase, axisymmetric elasticity solution was developed to predict the sensitivity of the stress state to the interphase material properties and temperatures used in the experimental studies. Reductions in the ratio of the maximum interfacial shear stress to the maximum fiber axial stress, $\frac{\sigma_{rz(max)}}{\sigma_{zz(max)}}$, were predicted for decreasing values of interphase modulus. Theoretical comparisons were made with the experimental observations of IFSS by calculating $\frac{\sigma_{rz(max)}}{\sigma_{zz(max)}}$ for the appropriate interphase properties and temperature ranges used in the experiments. Predictions which incorporated the change in modulus of both the matrix and interphase with temperature were in good agreement with the experimental trends. The theoretical calculations also supported the existence of a reduced glass transition in the uncoated samples.

Acknowledgments

The authors would like to acknowledge the support of the Office of Naval Research.

References

1. L. T. Drzal, *Advances in Polymer Science* **75,** 1 (1986).
2. A. Kelly and W. R. Tyson, *J. Mechanics and Physics of Solids* **13,** 329 (1965).

3. W. A. Fraser, F. H. Achker, and A. T. DiBenedetto, *Proceedings of 30th Annual Technical Conference of the SPE,* Paper 22-A (1975).
4. L. T. Drzal, M. J. Rich, J. D. Camping, and W. J. Park, *Proceedings of the 35th Annual Technical Conference of the Reinforced Plastics/Composites Institute,* Paper 20-C (1980).
5. L. T. Drzal, *SAMPE Journal* **19,** 7 (1983).
6. M. S. Madhukar and L. T. Drzal, *J. Composite Materials* **25,** 932 (1991).
7. M. S. Madhukar and L. T. Drzal, *J. Composite Materials* **25,** 958 (1991).
8. V. Rao and L. T. Drzal, *J. Adhesion* **37,** 83 (1991).
9. V. Rao and L. T. Drzal, *Polymer Composites* **12,** 48 (1991).
10. A. S. Wimolkiatisak and J. P. Bell, *Polymer Composites* **10,** 162 (1989).
11. T. Ohsawa, A. Nakayama, M. Miwa, and A. Hawegawa, *J. Appl. Polym. Sci.* **22,** 3203 (1978).
12. E. M. Asloun, M. Nardin and J. Schultz, *J. Mater. Sci.* **24,** 1835 (1989).
13. A. T. DiBenedetto, *Composites Science and Technology* **42,** 103 (1991).
14. P. S. Theocaris and G. C. Papanicolaou, *Fibre Science and Technology* **12,** 421 (1979).
15. N. R. Sottos, in *Polymer Solutions, Blends and Interfaces,* I. Noda and D. N. Rubingh, Eds. (Elsevier, Amsterdam, 1992), p. 339.
16. H. L. Cox, *Brit. J. Appl. Phys.* **3,** 72 (1952).
17. N. F. Dow, *Study of Stresses Near a Discontinuity in a Filament-Reinforced Composite Metal,* General Electric Company Report, TIS R63SD61 (1963).
18. B. W. Rosen, *Fibre Composite Materials* (American Society for Metals Publication, Metals Park, OH, 1965), p. 37.
19. A. Kelly and W. R. Tyson, *J. Mechanics and Physics of Solids* **13,** 199 (1965).
20. M. R. Piggott, *Load Bearing Fibre Composites* (Pergamon, Oxford, 1980), Chap. 5.
21. M. R. Piggott, *J. Mater. Sci.* **13,** 1709 (1978).
22. Th. Lacroix, B. Tilmans, R. Keunings, M. Desaeger, I. Verpoest, *Composite Science and Technology* **43,** 379 (1992).
23. J. M. Whitney and L. T. Drzal, *Toughened Composites,* ASTM STP 937, 179 (1987).
24. J. Haener, *Micromechanical Behavior of Fiber Reinforced Plastics.* Technical Report 66–62, *USAAVLABS,* AD-643813 (1966).
25. A. Levy, *Fiber-Matrix Interaction in a Composite Material.* Technical Report N70-24467, Grumman Research Department (1970).
26. J. A. Nairn, *Mechanics of Materials* **13,** 131 (1992).
27. A. S. Carrara and F. J. McGarry, *J. Composite Materials* **2,** 222 (1968).
28. Z. Maekawa, H. Hamada, S. Yoshioka, N. Ikuta, T. Tanimoto, T. Hirashim, in *Interfaces in Polymer, Ceramic and Metal Matrix Composites,* H. Ishida, Ed. (Elsevier, Amsterdam, 1988), p. 553.
29. F. C. Lhotellier and H. F. Brinson, *Composite Structures* **10,** 281 (1988).
30. P. J. Sabat, *Evaluation of the Fiber-Matrix Interfacial Shear Strength in Fiber Reinforced Plastics.* Masters Thesis, Virginia Polytechnic Institute and State University (1986).
31. R. Dave and L. Lorenzo, *Polymer Composites* **10,** 199 (1989).
32. N. R. Sottos, R. L. McCullough and W. R. Scott, *Composites Sciene and Technology* **44,** 319 (1992).
33. C. Galiotis, R. J. Young, P. H. J. Yeung and D. N. Batchelder, *J. Mater. Sci.* **19,** 3640 (1984).
34. G. R. Palmese and R. L. McCullough, *J. Appl. Polym. Sci.* **46,** 1863 (1992).

APPENDIX

The displacements and stresses associated with the particular solution (denoted by subscript p) are related to the displacement potential $\psi^{(i)}$ by

$$u_p^{(i)} = \frac{\partial \psi^{(i)}}{\partial r}$$

$$w_p^{(i)} = \frac{\partial \psi^{(i)}}{\partial z} \tag{A1}$$

$$\sigma_{rr\,p}^{(i)} = 2G^{(i)}\left(\frac{\partial^2 \psi^{(i)}}{\partial r^2} - \nabla^2 \psi^{(i)}\right)$$

$$\sigma^{(i)}_{\theta\theta\,p} = 2G^{(i)}\left(\frac{1}{r}\frac{\partial\psi^{(i)}}{\partial r} - \nabla^2\psi^{(i)}\right)$$

$$\sigma^{(i)}_{zz\,p} = 2G^{(i)}\left(\frac{\partial^2\psi^{(i)}}{\partial z^2} - \nabla^2\psi^{(i)}\right)$$

$$\sigma^{(i)}_{rz\,p} = 2G^{(i)}\frac{\partial^2\psi^{(i)}}{\partial r\partial z}$$

The complementary solutions for the displacements and stresses are of the form

$$u^{(i)}_c = -\frac{1+\nu^{(i)}}{E^{(i)}}\frac{\partial F^{(i)}}{\partial r\partial z}$$

$$w^{(i)}_c = \frac{1+\nu^{(i)}}{E^{(i)}}\left[2(1-\nu^{(i)})\nabla^2F^{(i)} - \frac{\partial^2F^{(i)}}{\partial z^2}\right]$$

$$\sigma^{(i)}_{rr\,c} = \frac{\partial}{\partial z}\left[\nu^{(i)}\nabla^2F^{(i)} - \frac{\partial^2F^{(i)}}{\partial r^2}\right] \tag{A2}$$

$$\sigma^{(i)}_{\theta\theta\,c} = \frac{\partial}{\partial z}\left[\nu^{(i)}\nabla^2F^{(i)} - \frac{1}{r}\frac{\partial F^{(i)}}{\partial r}\right]$$

$$\sigma^{(i)}_{zz\,c} = \frac{\partial}{\partial z}\left[(2-\nu^{(i)})\nabla^2F^{(i)} - \frac{\partial^2F^{(i)}}{\partial z^2}\right]$$

$$\sigma^{(i)}_{rz\,c} = \frac{\partial}{\partial z}\left[(1-\nu^{(i)})\nabla^2F^{(i)} - \frac{\partial^2F^{(i)}}{\partial z^2}\right]$$

where F(r,z) is Love's Function and the subscript, c, represents the complementary solution. The functions $h^{(i)}_{jn}$ and $g^{(i)}_{jn}$ where j = 1,2,...12 in Eq. (A2) can be expressed in terms of modified Bessel functions of the first and second kind I_0, I_1, K_0, K_1 and the engineering constants, E and ν, as follows:

$$h^{(i)}_{1n} = -\left(\frac{1+\nu^{(i)}}{E^{(i)}}\right)\mu_n^2 I_1(\mu_n r) \tag{A3}$$

$$h^{(i)}_{2n} = -\left(\frac{1+\nu^{(i)}}{E^{(i)}}\right)\mu_n^3 r I_0(\mu_n r) \tag{A4}$$

$$h^{(i)}_{3n} = \left(\frac{1+\nu^{(i)}}{E^{(i)}}\right)\mu_n^2 I_0(\mu_n r) \tag{A5}$$

$$h^{(i)}_{4n} = \left(\frac{1+\nu^{(i)}}{E^{(i)}}\right)\mu_n^2[4(1-\nu^{(i)})I_0(\mu_n r) + \mu_n r I_1(\mu_n r)] \tag{A6}$$

$$h^{(i)}_{5n} = \mu_n^2\left[-\mu_n I_0(\mu_n r) + \frac{1}{r}I_1(\mu_n r)\right] \tag{A7}$$

$$h^{(i)}_{6n} = \mu_n^3[(2\nu^{(i)}-1)I_0(\mu_n r) - \mu_n r I_1(\mu_n r)] \tag{A8}$$

$$h^{(i)}_{7n} = -\frac{\mu_n^2}{r}I_1(\mu_n r) \tag{A9}$$

$$h^{(i)}_{8n} = \mu_n^3(2\nu^{(i)}-1)I_0(\mu_n r) \tag{A10}$$

$$h_{9n}^{(i)} = \mu_n^3 I_0(\mu_n r) \tag{A11}$$

$$h_{10n}^{(i)} = \mu_n^3[2(2-\nu^{(i)})I_0(\mu_n r) + \mu_n r I_1(\mu_n r)] \tag{A12}$$

$$h_{11n}^{(i)} = \mu_n^3 I_1(\mu_n r) \tag{A13}$$

$$h_{12n}^{(i)} = \mu_n^3[\mu_n r I_0(\mu_n r) + 2(1-\nu^{(i)})I_1(\mu_n r)] \tag{A14}$$

$$g_{1n}^{(i)} = \left(\frac{1+\nu^{(i)}}{E^{(i)}}\right)\mu_n^2 K_1(\mu_n r) \tag{A15}$$

$$g_{2n}^{(i)} = \left(\frac{1+\nu^{(i)}}{E^{(i)}}\right)\mu_n^3 r K_0(\mu_n r) \tag{A16}$$

$$g_{3n}^{(i)} = \left(\frac{1+\nu^{(i)}}{E^{(i)}}\right)\mu_n^2 k_0(\mu_n r) \tag{A17}$$

$$g_{4n}^{(i)} = \left(\frac{1+\nu^{(i)}}{E^{(i)}}\right)\mu_n^2[-4(1-\nu^{(i)})K_0(\mu_n r) + \mu_n r K_1(\mu_n r)] \tag{A18}$$

$$g_{5n}^{(i)} = \mu_n^2\left[-\mu_n k_0(\mu_n r) - \frac{1}{r}K_1(\mu_n r)\right] \tag{A19}$$

$$g_{6n}^{(i)} = \mu_n^3[(1-2\nu^{(i)})K_0(\mu_n r) - \mu_n r K_1(\mu_n r)] \tag{A20}$$

$$g_{7n}^{(i)} = \frac{\mu_n^2}{r}K_1(\mu_n r) \tag{A21}$$

$$g_{8n}^{(i)} = \mu_n^3(1-2\nu^{(i)})K_0(\mu_n r) \tag{A22}$$

$$g_{9n}^{(i)} = \mu_n^3 K_0(\mu_n r) \tag{A23}$$

$$g_{10n}^{(i)} = \mu_n^3[-2(2-\nu^{(i)})K_0(\mu_n r) + \mu_n r K_1(\mu_n r)] \tag{A24}$$

$$g_{11n}^{(i)} = -\mu_n^3 K_1(\mu_n r) \tag{A25}$$

$$g_{12n}^{(i)} = \mu_n^3[-\mu_n r K_0(\mu_n r) + 2(1-\nu^{(i)})K_1(\mu_n r)] \tag{A26}$$